THE JOURNAL OF PHYSICAL CHEMISTRY Letters

Letter

pubs.acs.org/JPCL

Probing Photocurrent Nonuniformities in the Subcells of Monolithic Perovskite/Silicon Tandem Solar Cells

Zhaoning Song,[†] Jérémie Werner,[‡] Niraj Shrestha,[†] Florent Sahli,[‡] Stefaan De Wolf,[‡,⊥] Björn Niesen,[*,‡,§] Suneth C. Watthage,[†] Adam B. Phillips,[†] Christophe Ballif,[‡,§] Randy J. Ellingson,[†] and Michael J. Heben[*,†]

[†]Wright Center for Photovoltaics Innovation and Commercialization, Department of Physics and Astronomy, University of Toledo, 2801 West Bancroft Street, Toledo, Ohio 43606 United States

[‡]Institute of Microengineering (IMT), Photovoltaics and Thin-Film Electronics Laboratory (PV-Lab), Ecole Polytechnique Fédérale de Lausanne (EPFL), Rue de la Maladière 71b, 2002 Neuchâtel, Switzerland

[§]CSEM, PV-Center, Jaquet-Droz 1, 2002 Neuchâtel, Switzerland

Supporting Information

ABSTRACT: Perovskite/silicon tandem solar cells with high power conversion efficiencies have the potential to become a commercially viable photovoltaic option in the near future. However, device design and optimization is challenging because conventional characterization methods do not give clear feedback on the localized chemical and physical factors that limit performance within individual subcells, especially when stability and degradation is a concern. In this study, we use light beam induced current (LBIC) to probe photocurrent collection nonuniformities in the individual subcells of perovskite/silicon tandems. The choices of lasers and light biasing conditions allow efficiency-limiting effects relating to processing defects, optical interference within the individual cells, and the evolution of water-induced device degradation to be spatially resolved. The results reveal several types of microscopic defects and demonstrate that eliminating these and managing the optical properties within the multilayer structures will be important for future optimization of perovskite/silicon tandem solar cells.

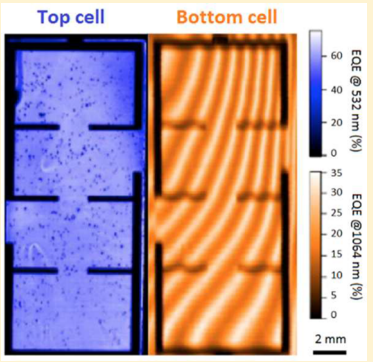

After more than 60 years of progress, photovoltaic (PV) solar cells, with a cumulative capacity of more than ∼260 GW, have become an economically viable means of generating electricity for the whole world.[1] To date, nearly all of the installed PV systems consist of single-junction solar cells based on either crystalline silicon or thin films [e.g., CdTe and $CuIn_{1-x}Ga_x(S,Se)_2$]. Continued research has allowed these PV technologies to provide power conversion efficiencies (PCEs) ranging from ∼12 to 25% at different cost-to-performance ratios.[2] Despite this and anticipated future progress, it is important to note that the PCE of single-junction solar cells cannot surpass the Shockley−Queisser limit of ∼33% under 1 sun illumination.[3] To become more competitive with conventional power generation technologies, a low-cost solution to boost the PCE of solar cells is needed. One viable approach is to develop two-junction tandem solar cells that can theoretically reach 42% efficiency under 1 sun illumination.[4] While a 1 sun efficiency of 38.8% has been demonstrated by a four-junction tandem cell based on III−V materials (e.g., GaInAs),[5] such materials may be practically limited to aerospace or concentrator PV applications due to extremely high manufacturing and materials costs. Widespread deployment of high-efficiency tandem PV technology will likely require thin-film materials that can be monolithically integrated and manufactured economically.

Among all of the promising candidates for thin-film PV technologies, organic−inorganic hybrid metal halide perovskites, such as methylammonium lead iodide ($CH_3NH_3PbI_3$), have attracted great attention in the past 5 years due to high single-junction device efficiencies (>22%),[6] simple fabrication processes,[7−10] and low manufacturing costs.[11−14] In addition, with a tunable band gap between 1.2 and 2.3 eV and low-temperature solution-processing routes,[15−19] there is great potential for monolithically integrating perovskite solar cells into commercially viable PV modules.

Recently, several different designs for perovskite tandem solar cells have been described with a wide-band-gap perovskite cell on top of a lower-band-gap cell comprised of crystalline silicon,[20−28] Cu chalcogenides,[20,29−32] polymers,[33] or another perovskite material.[34,35] Two and four terminal configurations with theoretical efficiencies well beyond 30% have been proposed,[36] with the former promising better light coupling and balance of system cost reductions while the latter offers flexibility of operation and construction. Among these, the two-terminal monolithic perovskite/Si tandem solar cell architecture may offer the best promise for near-term commercialization.

Received: October 17, 2016
Accepted: November 23, 2016
Published: November 23, 2016

DOI: 10.1021/acs.jpclett.6b02415
J. Phys. Chem. Lett. 2016, 7, 5114−5120

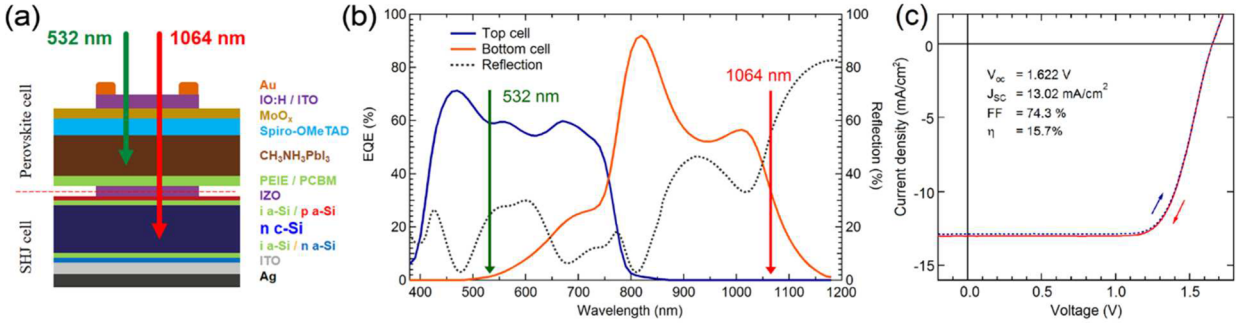

Figure 1. (a) Schematic of the monolithic perovskite/silicon tandem cell. (b) EQE and optical reflection spectra of a typical perovskite/SHJ tandem device. EQE spectra were obtained with light bias. (c) $J-V$ curve of the perovskite/SHJ tandem cell.

Device design, fabrication, and subcell compatibility are of major importance for producing high-performance, low-cost monolithic tandem solar cells. One constraint for monolithic tandem cells is that each subcell must generate the same current under a given operating condition; this is the so-called current matching requirement. This consideration affects layer thickness decisions and is conventionally applied at the subcell level, but it must also be considered at the microscopic level. For example, photocurrent nonuniformities due to processing defects and local areas containing weak diodes can limit the performance of a subcell and adversely impact current matching and, thus, the performance of the entire tandem device. Conventional characterization techniques such as current density−voltage ($J-V$) and external quantum efficiency (EQE) measurements focus on the overall PV response of the complete tandem or the individual subcells and yield area-integrated data. Processing defects and weak diodes in the tandem structure may be difficult to analyze and locate with these conventional tools, especially if there are subtle nonuniformities in current generation and collection in the solution-processed subcell.

Light beam induced current (LBIC) imaging has been demonstrated as a versatile method for identifying processing defects in cells and modules by spatially resolving the photocurrent generation and collection.[37−42] In the present contribution, we use LBIC to probe photocurrent nonuniformities in the individual subcells of perovskite/Si tandem solar cells. By using laser light at different wavelengths in combination with background light bias, we can identify processing defects and efficiency-limiting regions and provide in-depth quantitative analysis of current generation and transport in the individual subcells. The results provide critical feedback that is needed for device optimization.

Monolithic perovskite/crystalline silicon heterojunction (SHJ) tandem solar cells (Figure 1a), prepared as previously reported,[28] were used for this study. In brief, these tandem cells consisted of a front-emitter SHJ bottom cell based on a double-side-polished (DSP) wafer, an indium zinc oxide (IZO) intermediate recombination layer, and a $CH_3NH_3PbI_3$ perovskite top cell with polyethylenimine ethoxylated (PEIE)/phenyl-C60-butyric acid methyl ester (PCBM) and 2,2′,7,7′-tetrakis(*N*,*N*-di-4-methoxyphenylamino)-9,9′-spirobifluorene (spiro-OMeTAD) electron and hole transport layers, respectively. The transparent front electrode was composed of a MoO_x buffer layer and a bilayer of hydrogenated indium oxide (IO:H) and indium tin oxide (ITO). To quantify the photocurrent in the individual subcells, we measured the EQE of each subcell and the optical reflectance and $J-V$ curve of the entire device (Figures 1b,c). Some factors limiting the photocurrent of the subcells can be identified from the spectra. For the top cell, the overall EQE (∼70% maximum) is less than the state-of-art transparent perovskite cells (>80%),[27] likely due to the presence of defects in the solution-processed layers (vide infra). At longer wavelengths (>850 nm), strong optical interference effects give rise to modulations in the reflectivity with complementary reductions in the EQE.

To gain further insight, a custom LBIC system was used to spatially resolve current generation in the tandem cells.[42] Laser light at different wavelengths (532 and 1064 nm) and at a relatively low power density (∼800 mW/cm^2, to avoid possible illumination damage of the perovskite cell)[43] was used to excite charge carriers in the perovskite and Si subcells. The photogenerated current was calibrated for EQE to construct LBIC maps using a reference photodiode (Figure S1). A bias light with a controlled optical spectrum was applied to selectively generate carriers in only one of the subcells[44] so that the LBIC of the entire device was limited by the laser-generated current in the measured subcell (see the Experimental Methods section for details).

Figure 2 shows LBIC maps for a tandem device probed with a 532 nm laser with a background red (λ > 830 nm) or blue (λ < 450 nm) light bias. In the former case (Figure 2a), the top perovskite cell is current-limiting, while in the latter (Figure 2b), current generation in the perovskite cell is saturated so that current contributions from the Si bottom cell are limiting. The device area is surrounded by the black lines in the images, which correspond to areas shaded by the Au front grid electrode. Interestingly, photocurrent generated in the perovskite (top) cell is confined to the device area, whereas the Si (bottom) cell shows a decay of the photoresponse with distance outside of the Au grid (Figure 2b). In the latter case, the distance dependence of the photocurrent collection outside of the grid can provide a measure of the charge carrier diffusion length, which is long in the Si subcells (on the order of a few mm).[45]

Figure 2a,b shows areas with both higher (brighter) and lower (darker) EQE than the spatially averaged values. Qualitatively, variations due to, for example, layer thickness nonuniformities, processing defects, or impurities may be expected. Indeed, photoluminescence (PL) measurements at various spots across devices show significant variation in emission intensity (Figure S2). By considering the LBIC data in detail, more information can be gleaned. For example, Figure 2c,d shows the LBIC data for the top and bottom cells, respectively, at higher magnification from a region of the device where two common behaviors are observed.

DOI: 10.1021/acs.jpclett.6b02415
J. Phys. Chem. Lett. 2016, 7, 5114−5120

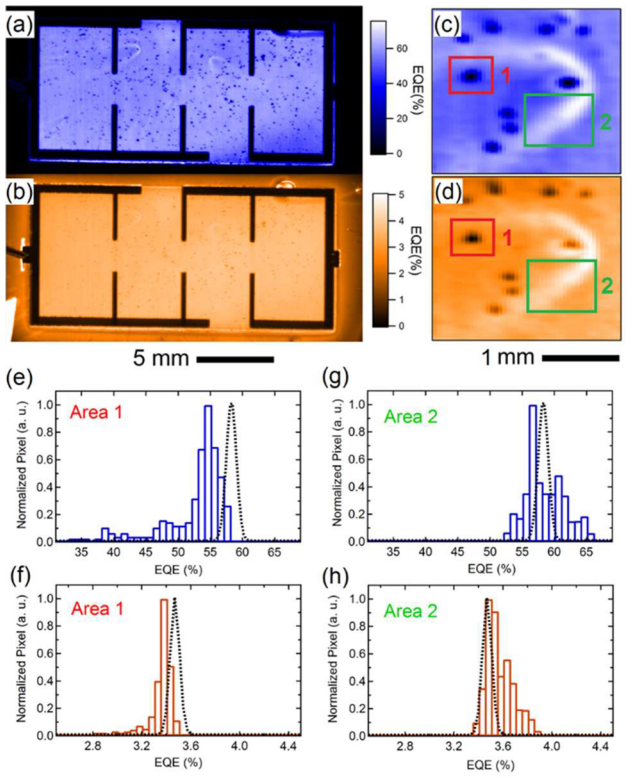

Figure 2. LBIC maps of the top (a,c) and bottom (b,d) cells of a typical perovskite/silicon tandem solar cell probed with a 532 nm laser light under red or blue light bias, respectively. Histograms of photocurrent distribution from two selected areas (1 and 2 in panels c and d) that show different behaviors for the top (e,g) and bottom (f,h) cells. The dashed curves in the histograms show the current distribution averaged across the device area.

Area 1 shows a common type of defect in which the photocurrent is reduced in both the top and bottom cells. These 100−200 μm features are ubiquitous. Note that the collection properties of the top cell and the interconnection between cells at the defect site are irrelevant to current collection from the bottom cell because the long carrier diffusion lengths in the Si would allow current to be collected away from the defect if the underlying Si were indeed photoexcited. Scanning electron microscopy and elemental analysis revealed several different types of defects (Figure S3), and each one was found to be deficient in either Pb, Si, N, or I. We can speculate that the defect in Area 1 is related to a light-blocking impurity particle or component aggregate that was introduced during solution-based processing of the PEIE/PCBM, spiro-OMeTAD, or perovskite layers. It is unlikely that such a large particle could be introduced through the air during processing because the samples are handled in a clean room environment. Figure 2e,f shows distribution histograms for the LBIC data from Area 1 in comparison to the area-averaged data for the device. Clearly, higher performance for the tandem could be achieved if these defects could be eliminated. This might be achieved by simply adjusting the solubility/viscosity of the solution or by filtering prior to deposition.

Area 2 in Figure 2c,d shows another type of behavior. Here, a comet streak is seen where the EQE is enhanced in both the top and bottom cells. At least eight features like this are observed in Figure 2a,b. The orientation of the features, with the half-ellipse pointing toward the rotational axis of the sample during spinning, makes it clear that these features are developed during a spinning process. Possible origins include height variation in an underlying layer that could affect the hydrodynamics of material distribution during a spinning step or use of a precursor solution with nonuniform viscosity. Variations in the perovskite film thickness are not expected to be responsible for this behavior because such variations should impact the EQE from the top and bottom cells oppositely, as explained below. Thus, we are left with assigning the features to behavior associated with spinning application of the spiro-OMeTAD. Note that the comet-shaped defect is anchored on a defect like the one found in Area 1. Interestingly, the thickness variation of the spiro-OMeTAD creates a local variation in the film thickness, as shown in the optical microscopic image (Figure S4). Clearly, more study of these "defects" is warranted; the data in Figure 2h,g suggest that the overall device efficiency could be significantly enhanced if the EQE benefits could be harvested across the entire device area.

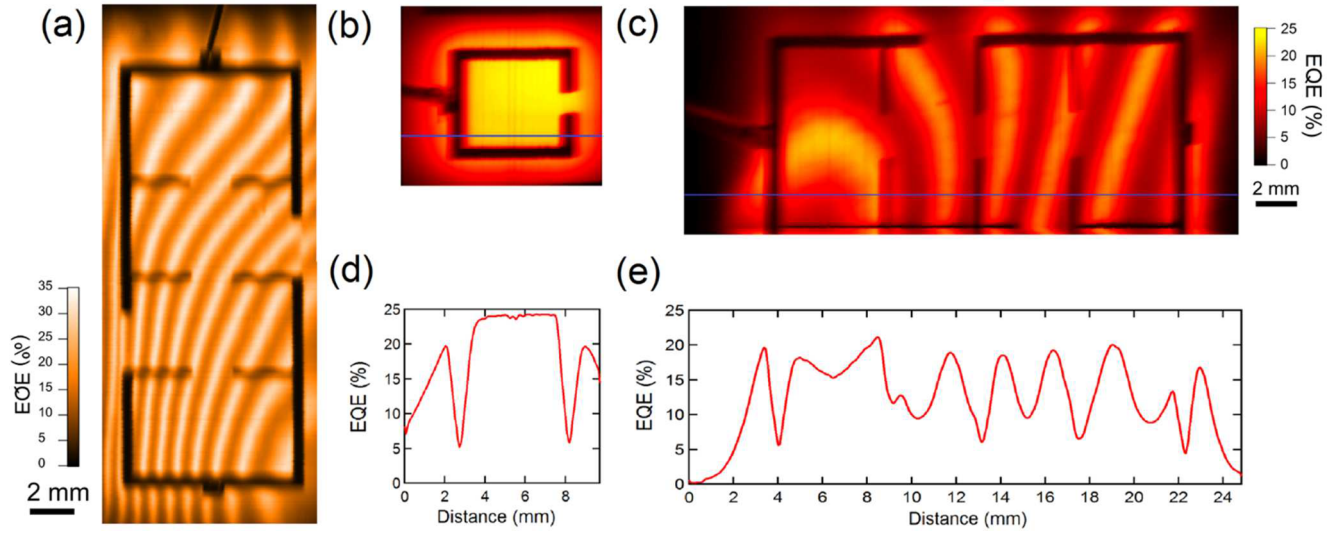

Figure 3. LBIC maps taken with 1064 nm laser light under blue light bias of a (a) perovskite/Si tandem, (b) SST Si single-junction device, and (c) DSP Si single-junction device. Also shown are line scan signals across the (d) SST Si and (e) DSP Si devices.

DOI: 10.1021/acs.jpclett.6b02415
J. Phys. Chem. Lett. 2016, 7, 5114−5120

Another type of defect (Figure S5) shows a local reduction in the photocurrent in the top cell and a corresponding increase in the bottom cell. This can be explained by considering that the solution-processed perovskite layer may be locally thin, missing, or degraded,[37,46] such that light absorption in the perovskite cell is decreased. Reduced absorption in the top cell would allow more light to pass through, leading to more photocurrent generation in the bottom cell. Additionally, reduced thickness or incomplete coverage of the perovskite layer may introduce local shunts in the top cell, improving the transport of charge carriers generated in the bottom cell. To ameliorate this type of defect, the formation of a compact and phase-pure perovskite layer should be precisely controlled.[46]

Similar LBIC analyses were performed on other devices with small (0.17 cm^2) and large (1.22 cm^2) areas (Figures S6 and S7). As expected, the large-area devices generally exhibited more severe current nonuniformities than the smaller ones. Quantifying the LBIC results shows that if all top cell defects could be eliminated by optimization of the processing and optical design, the overall current generation in the perovskite cell could be improved by up to 3 mA/cm^2, which would boost the efficiency of that tandem cell from ∼16 to ∼19% (Figure S8)

The LBIC maps obtained with the 1064 nm laser reveal new, interesting behaviors (Figure 3a). No signal was collected from the top cell because the perovskite subcell is transparent to 1064 nm light. In the bottom cell, however, although there is evidence for the same defects observed using the 532 nm laser light (Figure 2d), optical interference fringes were dominant (Figure 3a). The patterns persisted after the sample was rotated or moved relative to the laser beam's axis (Figure S9), indicating that the optical fringes originated from the device structure. The fringes are most likely caused by the nonparallelism of the two mirror polished surfaces of the silicon bottom cell.[45] Analysis of the optical path length between adjacent maxima shows that the nonparallelism from fringe maximum to fringe maximum is ∼0.6 μm (Supporting Information). This variation arises due to the particular DSP Si wafers (260−300 μm thickness) that were used with a specified total thickness variation of 5−10 μm across wafers.

To confirm the origin of the optical fringes, we compared the LBIC maps of two SHJ cells that were prepared with single-side-textured (SST) and DSP surfaces. It is notable that the bottom cells with front surface texture are not currently compatible with solution processing of the perovskite cells; thus, only the back surface of the SHJ cell can be textured with random pyramids. The SST cell (Figure 3b) exhibits a high and uniform photocurrent over the active area. The DSP cell (Figure 3c), on the contrary, shows optical interference patterns similar to those of the perovskite/Si tandem device. To quantify the photocurrent nonuniformities caused by optical interference of the bottom cells, the line scan profiles of these two devices are shown in Figure 3d,e. The peak-to-peak variations of photocurrent generated by the 1064 nm laser in the SST and DSP cells are 5 and 36%, respectively. The large variation in the DSP cell indicates that the tandem devices using the DSP bottom cells suffer a significant monochromatic efficiency loss due to the absence of light trapping, which is qualitatively consistent with the EQE spectra of the tandem device (Figure 1b). This optical loss can be recovered by the addition of an antireflective coating (e.g., MgF_2) or micro-textured foil[47] to the device and/or the use of the textured back surface of bottom cells.[27]

To study the evolution of the efficiency-limiting defects in perovskite/Si tandem solar cells, the LBIC maps were collected in situ under controlled humidity conditions (relative humidity, RH, of 80%) using the 532 nm laser. The behavior of the top cell degradation (Figure S10) measured under red light bias is similar to that observed for single-junction perovskite devices.[37] The performance of the perovskite cell rapidly degraded after exposure to humid air due to the formation of the monohydrated perovskite phase. Interesting behavior was observed without light bias when the tandem cell was aged under the controlled humidity condition (Figure 4). When

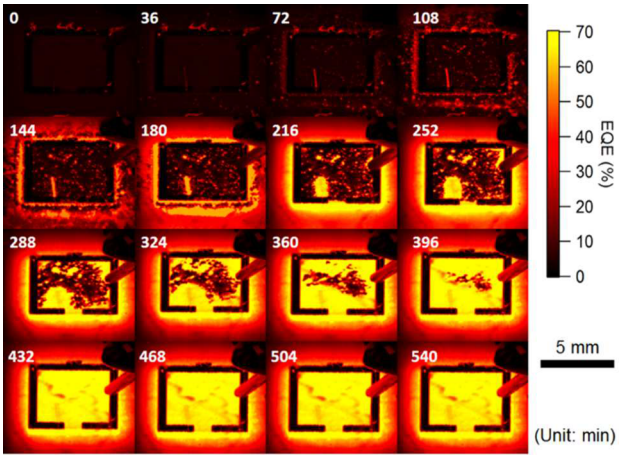

Figure 4. Evolution of the LBIC map at 532 nm without light bias of a perovskite/Si tandem device after exposure to humid air (80% RH).

measured by the 532 nm laser, a fresh tandem device showed ∼3% EQE, which was mainly limited by the current match to the Si bottom cell. Specifically, due to high optical absorption in the top cell, only a small number of photons can enter the bottom cell and generate photocurrent. However, after exposure to humidity, the perovskite material started to react with water and transform into the monohydrate perovskite phase.[37] This phase transition changed the band gap of the perovskite material from ∼1.55 to ∼3.1 eV,[48] and consequently, the light transmission through the perovskite layer increased. Surprisingly, the 532 nm EQE of the entire device increased up to ∼70% after hydration of the perovskite, indicating that the perovskite subcell became a transparent conducting film stack, enabling efficient collection of photocurrent current generated in the SHJ bottom cell. Our preliminary resistance measurements of perovskite films reveal that the conductivity of the films increased by ∼30 times after exposure to humid air for 60 min (Figure S11). Further investigation is ongoing to reveal the evolution of the electrical properties of the perovskite cells. In addition to the LBIC mapping, electroluminescence (EL) measurements also show an emission peak shift from 770 to 1050 nm after degradation of the perovskite cell, corresponding to the change of performance dominating the junction from the perovskite to the Si cell (Figure S12).

Looking into the details of the evolution of the defects, the EQE changes originate at regions outside of the active device area. These regions are not covered by the transparent electrode and, thus, are more prone to moisture ingress. Additionally, a significant change in the EQE is observed close to the scratch at the left bottom side of the device. As the exposure time was increased, the degradation front propagated toward the center of the device and the perovskite cell was

DOI: 10.1021/acs.jpclett.6b02415
J. Phys. Chem. Lett. 2016, 7, 5114−5120

completely degraded after ~480 min. The observations are consistent with recent findings by Bush et al. that show that the impacts of moisture can be mitigated to some degree by combining a compact ITO layer, a hydrophobic charge transport layer, and more stable perovskite compositions.[24]

In summary, we used LBIC combined with light bias to probe photocurrent nonuniformities within the subcells of high-efficiency perovskite/Si tandem devices. A variety of phenomena including light-blocking, defects, and potential enhancements were observed. Strong optical interference introduced by 1064 nm laser light was observed when DSP bottom cells were used. This optical loss can be mitigated by developing tandems on the textured SHJ cells. Additionally, we observed the evolution of a LBIC map of a tandem device after exposure to humid air, showing the importance of protecting the device from water ingress. For full realization of the promise of high-efficiency perovskite/Si tandems, management of the material uniformity, interface integrity, current collection and generation, and optics of the interfaces and layers will be essential.

EXPERIMENTAL METHODS

Device Fabrication. The perovskite/silicon tandem solar cells were fabricated following a previously published method.[28] In brief, a DSP n-type-doped silicon wafer was used to prepare a SHJ solar cell, serving as the bottom cell for the tandems. A 40 nm IZO was sputtered on the front side of the silicon bottom cells to act as a recombination layer. Then, the perovskite top cell was deposited as follows. The electron contact was prepared by spin-coating of a PEIE/PCBM bilayer. The perovskite absorber layer was fabricated with a hybrid sequential method, consisting of an evaporated 150 nm PbI_2 layer subsequently transformed in the perovskite phase by spin coating a 50 mg/mL methylammonium iodide solution. The hole contact was prepared by spin coating of spiro-OMeTAD solution. The transparent front electrode was deposited by thermal evaporation of a 10 nm MoO_x buffer layer, followed by sputtering of a bilayer of 110 nm IO:H/ITO. A 100 nm gold frame was finally evaporated through a shadow mask.

LBIC Measurement. The LBIC system as previously reported was used to spatially resolve the current collection efficiency map.[42] Nd:YAG lasers at 532 and 1064 nm operating in the Q-switching mode were used to generate a light beam with an average power of 0.01 mW and a 40 μm diameter. The laser beam was used to scan across the tandem solar cells at a speed of 1 mm/s with a 30 μm spacing between two lateral scans. The photocurrent was collected by a Keithley 2601 source meter at an acquisition rate of 5 kHz and converted into local external quantum efficiencies using a reference Si photodiode (Model: S2281-8D083) with a calibrated EQE (Figure S1). The top/bottom cell was measured with infrared/blue (λ > 830 nm/< 450 nm) light bias generated using a white 100 W light source with the corresponding long/short wavelength pass optical filter. The procedure for the in situ degradation study was similar to that in our previous work.[37]

Other Characterization Methods. EQE spectra were obtained from 320 to 1150 nm (PV Measurements IVQUE8-C) with the same light bias conditions as that in the LBIC measurements. *J*−*V* curves were measured using a Keithley 2440 source meter and a solar simulator (Newport model 91195A-1000) calibrated to simulate AM1.5 illumination. The optical reflection spectrum was measured by a UV−vis spectrometer (PerkinElmer Lambda 1050) in the range of 350−2000 nm. Scanning electron microscopic (SEM) images and energy-dispersive X-ray (EDX) spectroscopy were obtained using a field emission electron microscope (Hitachi S-4800). The PL/EL measurements were recorded (integration time = 0.5 s) by a Horiba Symphony-II CCD detector after a 300 g/mm grating monochromator (iHR-320). For PL measurement, a 532 nm cw laser beam (beam diameter ≈ 84 μm) at 79 mW/cm^2 was used as a source of excitation for steady state. For EL measurement, a tandem solar cell was forward biased while monitoring the applied voltage. The resistance of the perovskite films was measured using a Keithley 2601 source meter by sweeping the voltage from −20 to 20 V and recording the current.

ASSOCIATED CONTENT

Supporting Information

The Supporting Information is available free of charge on the ACS Publications website at DOI: 10.1021/acs.jpclett.6b02415.

LBIC to EQE calibration; PL spectra; SEM and EDX analysis on defects; LBIC analysis of a particular defect; LBIC maps of cells with different areas; LBIC statistics of cells with different areas; quantifying the potential current improvement; LBIC maps of optical interference; interference path length calculation; degradation of the perovskite top cell; resistivity evolution of a perovskite film; EL of tandem cells before and after degradation (PDF)

AUTHOR INFORMATION

Corresponding Authors

*E-mail: Bjoern.Niesen@csem.ch (B.N.).
*E-mail: Michael.Heben@utoledo.edu (M.J.H.).

ORCID

Zhaoning Song: 0000-0002-6677-0994
Michael J. Heben: 0000-0002-3788-3471

Present Address

⊥S.D.W.: King Abdullah University of Science and Technology (KAUST), KAUST Solar Center (KSC), Thuwal 23955-6900, Saudi Arabia.

Notes

The authors declare no competing financial interest.

ACKNOWLEDGMENTS

This work is financially supported by the Wright Center Endowment for Photovoltaics Innovation and Commercialization, U.S. Air Force Research Laboratory, Space Vehicles Directorate (Contract No. FA9453-11-C-0253), U.S. National Science Foundation (Contract No. CHE-1230246), Swiss National Science Foundation, Nano-Tera.ch, and Swiss Federal Office of Energy, under Grant SI/501072-01.

REFERENCES

(1) *Fraunhofer Institute for Solar Energy Systems Photovoltaic Report.* https://www.ise.fraunhofer.de/en/downloads-englisch/pdf-files-englisch/photovoltaics-report-slides.pdf (accessed 11 October 2016).
(2) Jean, J.; Brown, P. R.; Jaffe, R. L.; Buonassisi, T.; Bulovic, V. Pathways for Solar Photovoltaics. *Energy Environ. Sci.* **2015**, *8*, 1200−1219.
(3) Shockley, W.; Queisser, H. J. Detailed Balance Limit of Efficiency of p-n Junction Solar Cells. *J. Appl. Phys.* **1961**, *32*, 510−519.
(4) Vos, A. D. Detailed Balance Limit of the Efficiency of Tandem Solar Cells. *J. Phys. D: Appl. Phys.* **1980**, *13*, 839.

DOI: 10.1021/acs.jpclett.6b02415
J. Phys. Chem. Lett. 2016, 7, 5114−5120

(5) Green, M. A.; Emery, K.; Hishikawa, Y.; Warta, W.; Dunlop, E. D. Solar Cell Efficiency Tables (Version 48). *Prog. Photovoltaics* **2016**, *24*, 905−913.
(6) Yang, W. S.; Noh, J. H.; Jeon, N. J.; Kim, Y. C.; Ryu, S.; Seo, J.; Seok, S. I. High-Performance Photovoltaic Perovskite Layers Fabricated through Intramolecular Exchange. *Science* **2015**, *348*, 1234−1237.
(7) Lee, M. M.; Teuscher, J.; Miyasaka, T.; Murakami, T. N.; Snaith, H. J. Efficient Hybrid Solar Cells Based on Meso-Superstructured Organometal Halide Perovskites. *Science* **2012**, *338*, 643−647.
(8) Burschka, J.; Pellet, N.; Moon, S.-J.; Humphry-Baker, R.; Gao, P.; Nazeeruddin, M. K.; Graetzel, M. Sequential Deposition as a Route to High-Performance Perovskite-Sensitized Solar Cells. *Nature* **2013**, *499*, 316−319.
(9) Song, Z.; Watthage, S. C.; Phillips, A. B.; Heben, M. J. Pathways toward High-Performance Perovskite Solar Cells: Review of Recent Advances in Organo-Metal Halide Perovskites for Photovoltaic Applications. *J. Photonics Energy* **2016**, *6*, 022001.
(10) Li, X.; Bi, D.; Yi, C.; Décoppet, J.-D.; Luo, J.; Zakeeruddin, S. M.; Hagfeldt, A.; Grätzel, M. A Vacuum Flash−Assisted Solution Process for High-Efficiency Large-Area Perovskite Solar Cells. *Science* **2016**, *353*, 58.
(11) Snaith, H. J. Perovskites: The Emergence of a New Era for Low-Cost, High-Efficiency Solar Cells. *J. Phys. Chem. Lett.* **2013**, *4*, 3623−3630.
(12) Gao, P.; Gratzel, M.; Nazeeruddin, M. K. Organohalide Lead Perovskites for Photovoltaic Applications. *Energy Environ. Sci.* **2014**, *7*, 2448−2463.
(13) Green, M. A.; Ho-Baillie, A.; Snaith, H. J. The Emergence of Perovskite Solar Cells. *Nat. Photonics* **2014**, *8*, 506−514.
(14) Gong, J.; Darling, S. B.; You, F. Perovskite Photovoltaics: Life-Cycle Assessment of Energy and Environmental Impacts. *Energy Environ. Sci.* **2015**, *8*, 1953−1968.
(15) Zhang, W.; Anaya, M.; Lozano, G.; Calvo, M. E.; Johnston, M. B.; Míguez, H.; Snaith, H. J. Highly Efficient Perovskite Solar Cells with Tunable Structural Color. *Nano Lett.* **2015**, *15*, 1698−1702.
(16) Sutton, R. J.; Eperon, G. E.; Miranda, L.; Parrott, E. S.; Kamino, B. A.; Patel, J. B.; Hörantner, M. T.; Johnston, M. B.; Haghighirad, A. A.; Moore, D. T.; et al. Bandgap-Tunable Cesium Lead Halide Perovskites with High Thermal Stability for Efficient Solar Cells. *Adv. Energy Mater.* **2016**, *6*, 1502458.
(17) Xing, G.; Mathews, N.; Lim, S. S.; Yantara, N.; Liu, X.; Sabba, D.; Gratzel, M.; Mhaisalkar, S.; Sum, T. C. Low-Temperature Solution-Processed Wavelength-Tunable Perovskites for Lasing. *Nat. Mater.* **2014**, *13*, 476−480.
(18) Noh, J. H.; Im, S. H.; Heo, J. H.; Mandal, T. N.; Seok, S. I. Chemical Management for Colorful, Efficient, and Stable Inorganic-Organic Hybrid Nanostructured Solar Cells. *Nano Lett.* **2013**, *13*, 1764−1769.
(19) Liao, W.; Zhao, D.; Yu, Y.; Shrestha, N.; Ghimire, K.; Grice, C. R.; Wang, C.; Xiao, Y.; Cimaroli, A. J.; Ellingson, R. J.; et al. Fabrication of Efficient Low-Bandgap Perovskite Solar Cells by Combining Formamidinium Tin Iodide with Methylammonium Lead Iodide. *J. Am. Chem. Soc.* **2016**, *138*, 12360−12363.
(20) Bailie, C. D.; Christoforo, M. G.; Mailoa, J. P.; Bowring, A. R.; Unger, E. L.; Nguyen, W. H.; Burschka, J.; Pellet, N.; Lee, J. Z.; Gratzel, M.; et al. Semi-Transparent Perovskite Solar Cells for Tandems with Silicon and CIGS. *Energy Environ. Sci.* **2015**, *8*, 956−963.
(21) Mailoa, J. P.; Bailie, C. D.; Johlin, E. C.; Hoke, E. T.; Akey, A. J.; Nguyen, W. H.; McGehee, M. D.; Buonassisi, T. A 2-Terminal Perovskite/Silicon Multijunction Solar Cell Enabled by a Silicon Tunnel Junction. *Appl. Phys. Lett.* **2015**, *106*, 121105.
(22) Loper, P.; Moon, S.-J.; Martin de Nicolas, S.; Niesen, B.; Ledinsky, M.; Nicolay, S.; Bailat, J.; Yum, J.-H.; De Wolf, S.; Ballif, C. Organic-Inorganic Halide Perovskite/Crystalline Silicon Four-Terminal Tandem Solar Cells. *Phys. Chem. Chem. Phys.* **2015**, *17*, 1619−1629.
(23) Albrecht, S.; Saliba, M.; Correa Baena, J. P.; Lang, F.; Kegelmann, L.; Mews, M.; Steier, L.; Abate, A.; Rappich, J.; Korte, L.; et al. Monolithic Perovskite/Silicon-Heterojunction Tandem Solar Cells Processed at Low Temperature. *Energy Environ. Sci.* **2016**, *9*, 81−88.
(24) Bush, K. A.; Bailie, C. D.; Chen, Y.; Bowring, A. R.; Wang, W.; Ma, W.; Leijtens, T.; Moghadam, F.; McGehee, M. D. Thermal and Environmental Stability of Semi-Transparent Perovskite Solar Cells for Tandems Enabled by a Solution-Processed Nanoparticle Buffer Layer and Sputtered Ito Electrode. *Adv. Mater.* **2016**, *28*, 3937−3943.
(25) Chen, B.; Bai, Y.; Yu, Z.; Li, T.; Zheng, X.; Dong, Q.; Shen, L.; Boccard, M.; Gruverman, A.; Holman, Z.; et al. Efficient Semi-transparent Perovskite Solar Cells for 23.0%-Efficiency Perovskite/Silicon Four-Terminal Tandem Cells. *Adv. Energy Mater.* **2016**, *6*, 1601128.
(26) McMeekin, D. P.; Sadoughi, G.; Rehman, W.; Eperon, G. E.; Saliba, M.; Hörantner, M. T.; Haghighirad, A.; Sakai, N.; Korte, L.; Rech, B.; et al. A Mixed-Cation Lead Mixed-Halide Perovskite Absorber for Tandem Solar Cells. *Science* **2016**, *351*, 151−155.
(27) Werner, J.; Barraud, L.; Walter, A.; Bräuninger, M.; Sahli, F.; Sacchetto, D.; Tétreault, N.; Paviet-Salomon, B.; Moon, S.-J.; Allebé, C.; et al. Efficient near-Infrared-Transparent Perovskite Solar Cells Enabling Direct Comparison of 4-Terminal and Monolithic Perovskite/Silicon Tandem Cells. *ACS Energy Lett.* **2016**, *1*, 474−480.
(28) Werner, J.; Weng, C.-H.; Walter, A.; Fesquet, L.; Seif, J. P.; De Wolf, S.; Niesen, B.; Ballif, C. Efficient Monolithic Perovskite/Silicon Tandem Solar Cell with Cell Area > 1 cm^2. *J. Phys. Chem. Lett.* **2016**, *7*, 161−166.
(29) Todorov, T.; Gershon, T.; Gunawan, O.; Sturdevant, C.; Guha, S. Perovskite-Kesterite Monolithic Tandem Solar Cells with High Open-Circuit Voltage. *Appl. Phys. Lett.* **2014**, *105*, 173902.
(30) Todorov, T.; Gershon, T.; Gunawan, O.; Lee, Y. S.; Sturdevant, C.; Chang, L.-Y.; Guha, S. Monolithic Perovskite-CIGS Tandem Solar Cells via in situ Band Gap Engineering. *Adv. Energy Mater.* **2015**, *5*, 1500799.
(31) Kranz, L.; Abate, A.; Feurer, T.; Fu, F.; Avancini, E.; Löckinger, J.; Reinhard, P.; Zakeeruddin, S. M.; Grätzel, M.; Buecheler, S.; et al. High-Efficiency Polycrystalline Thin Film Tandem Solar Cells. *J. Phys. Chem. Lett.* **2015**, *6*, 2676−2681.
(32) Fu, F.; Feurer, T.; Jager, T.; Avancini, E.; Bissig, B.; Yoon, S.; Buecheler, S.; Tiwari, A. N. Low-Temperature-Processed Efficient Semi-Transparent Planar Perovskite Solar Cells for Bifacial and Tandem Applications. *Nat. Commun.* **2015**, *6*, 8932.
(33) Liu, Y.; Renna, L. A.; Bag, M.; Page, Z. A.; Kim, P.; Choi, J.; Emrick, T.; Venkataraman, D.; Russell, T. P. High Efficiency Tandem Thin-Perovskite/Polymer Solar Cells with a Graded Recombination Layer. *ACS Appl. Mater. Interfaces* **2016**, *8*, 7070−7076.
(34) Yang, Z.; Rajagopal, A.; Chueh, C.-C.; Jo, S. B.; Liu, B.; Zhao, T.; Jen, A. K. Y. Stable Low-Bandgap Pb−Sn Binary Perovskites for Tandem Solar Cells. *Adv. Mater.* **2016**, *28*, 8990−8997.
(35) Eperon, G. E.; Leijtens, T.; Bush, K. A.; Green, T.; Wang, J. T.-W.; McMeekin, D. P.; Volonakis, G. Perovskite-Perovskite Tandem Photovoltaics with Ideal Bandgaps. *ArXiv* 2016, https://arxiv.org/abs/1608.03920.
(36) Bailie, C. D.; McGehee, M. D. High-Efficiency Tandem Perovskite Solar Cells. *MRS Bull.* **2015**, *40*, 681−686.
(37) Song, Z.; Abate, A.; Watthage, S. C.; Liyanage, G. K.; Phillips, A. B.; Steiner, U.; Graetzel, M.; Heben, M. J. Perovskite Solar Cell Stability in Humid Air: Partially Reversible Phase Transitions in the PbI_2-CH_3NH_3I-H_2O System. *Adv. Energy Mater.* **2016**, *6*, 1600846.
(38) Vorasayan, P.; Betts, T. R.; Tiwari, A. N.; Gottschalg, R. Multi-Laser LBIC System for Thin Film PV Module Characterisation. *Sol. Energy Mater. Sol. Cells* **2009**, *93*, 917−921.
(39) Krebs, F. C.; Jørgensen, M. 2D Characterization of OPV from Single and Tandem Cells to Fully Roll-to-Roll Processed Modules with and without Electrical Contact. *Adv. Opt. Mater.* **2014**, *2*, 465−477.
(40) Larsen-Olsen, T. T.; Andersen, T. R.; Dam, H. F.; Jørgensen, M.; Krebs, F. C. Probing Individual Subcells of Fully Printed and

DOI: 10.1021/acs.jpclett.6b02415
J. Phys. Chem. Lett. 2016, 7, 5114−5120

Coated Polymer Tandem Solar Cells Using Multichromatic Opto-Electronic Characterization Methods. *Sol. Energy Mater. Sol. Cells* **2015**, *137*, 154−163.
(41) Reinhardt, J.; Apilo, P.; Zimmermann, B.; Rousu, S.; Würfel, U. Determining the Photocurrent of Individual Cells within an Organic Solar Module by LBIC and the Filtering Approach: Experiments and Simulations. *Sol. Energy Mater. Sol. Cells* **2015**, *134*, 157−164.
(42) Phillips, A. B.; Song, Z.; DeWitt, J. L.; Stone, J. M.; Krantz, P. W.; Royston, J. M.; Zeller, R. M.; Mapes, M. R.; Roland, P. J.; Dorogi, M. D.; et al. High Speed, Intermediate Resolution, Large Area Laser Beam Induced Current Imaging and Laser Scribing System for Photovoltaic Devices and Modules. *Rev. Sci. Instrum.* **2016**, *87*, 093708.
(43) Ledinský, M.; Löper, P.; Niesen, B.; Holovský, J.; Moon, S.-J.; Yum, J.-H.; De Wolf, S.; Fejfar, A.; Ballif, C. Raman Spectroscopy of Organic−Inorganic Halide Perovskites. *J. Phys. Chem. Lett.* **2015**, *6*, 401−406.
(44) Meusel, M.; Baur, C.; Létay, G.; Bett, A. W.; Warta, W.; Fernandez, E. Spectral Response Measurements of Monolithic GaInP/Ga(In)As/Ge Triple-Junction Solar Cells: Measurement Artifacts and Their Explanation. *Prog. Photovoltaics* **2003**, *11*, 499−514.
(45) Holovský, J.; De Wolf, S.; Jiříček, P.; Ballif, C. Attenuated Total Reflectance Fourier-Transform Infrared Spectroscopic Investigation of Silicon Heterojunction Solar Cells. *Rev. Sci. Instrum.* **2015**, *86*, 073108.
(46) Song, Z.; Watthage, S. C.; Phillips, A. B.; Tompkins, B. L.; Ellingson, R. J.; Heben, M. J. Impact of Processing Temperature and Composition on the Formation of Methylammonium Lead Iodide Perovskites. *Chem. Mater.* **2015**, *27*, 4612−4619.
(47) Ulbrich, C.; Gerber, A.; Hermans, K.; Lambertz, A.; Rau, U. Analysis of Short Circuit Current Gains by an Anti-Reflective Textured Cover on Silicon Thin Film Solar Cells. *Prog. Photovoltaics* **2013**, *21*, 1672−1681.
(48) Leguy, A. M. A.; Hu, Y.; Campoy-Quiles, M.; Alonso, M. I.; Weber, O. J.; Azarhoosh, P.; van Schilfgaarde, M.; Weller, M. T.; Bein, T.; Nelson, J.; et al. Reversible Hydration of $CH_3NH_3PbI_3$ in Films, Single Crystals, and Solar Cells. *Chem. Mater.* **2015**, *27*, 3397−3407.

DOI: 10.1021/acs.jpclett.6b02415
J. Phys. Chem. Lett. 2016, 7, 5114−5120